PAPER

Check for updates

Tunable large-scale regular array of topological defects in nematic liquid crystals†

MinSu Kim [ID] and Francesca Serra [ID] *

Arrays of topological defects in liquid crystals are fascinating systems, as isotropic and anisotropic phases of the same material can co-exist and be arranged in regular periodic structures. The arrays thus form spatially-varying optical pathways, in patterns that can be used for optics, as novel photonic structures, optical gratings, lenses or metamaterials, and for molecular and colloidal self-assembly. However, for practical applications, it is necessary that the arrays are tunable without direct intervention of the experimenters. Here, we demonstrate single-domain, tunable arrays of topological defects in nematic liquid crystals, using a method inspired by the recent work by Orihara and colleagues. The regularity and domain size of the defect arrays are obtained by using periodic lateral modulation of electric fields generated by incompletely etched electrodes with periodic conductivity. The period of the arrays, *i.e.* the characteristic spacing between defects, is controllable not only through the applied electric field strength and frequency but also by varying the size of the patterned electrodes. We believe these results open a new way to design and fabricate large-scale, single-domain, tunable and scalable device architectures that are optically functional.

Introduction

Spontaneous formation of periodic or regular patterns is ubiquitous in nature. Self and directed assembly are powerful tools to mimic nature and create patterns using soft materials, such as block-copolymers,[1,2] colloids[3,4] and liquid crystals (LCs).[5] Among these systems, LCs are useful as they form topological defects, special regions where the LC orientational order is not defined. One can generate defects by surface treatments,[6,7] geometric confinements,[8,9] or various external stimuli, such as electric field or flow.[10] Defect arrays can be used for optics, as arrays of optical vortices,[11,12] gratings,[13] micro-lens arrays,[14] or for other purposes such as templating super hydrophobic surfaces[6] or programming the 3D shape of LC elastomers.[15–17] However, realizing a regular, periodic array of defects is a nontrivial task and it often requires local manipulation by the experimenter, *e.g.* with optical or magnetic tweezers and complicated surface treatment,[18] combined with heat convection[19] or electric fields.[20–22]

One strategy is to exploit the Helfrich-like instability, caused by the electro-hydrodynamic effects in nematic LCs.[23–25] The conductivity properties of the LC, combined with the dielectric properties and the initial alignment determine what pattern will be formed when the instability occurs. The instability can

generate arbitrarily large two-dimensional patterns where an electric field is applied, but this pattern is generally irregular. This is due in part to the imperfect cleanliness of the surfaces of the LC cell and in part to the presence of ions, which are necessary for the formation of the pattern but whose behavior is difficult to control.

Recently, Orihara's group reported creating two-dimensional grid-like patterns in which umbilical defects with topological charges ±1 are formed near the top and bottom substrates.[21] The system consists of LCs with negative dielectric anisotropy with added ions, aligned homeotropically by using an amorphous fluoropolymer with high-resistivity. When AC field is applied under certain conditions a square array of umbilical defects appears (ESI Fig. S1a and b†). In general, this array is highly irregular. The authors outline two strategies to make the pattern uniform:[21] (1) electrodes are patterned into thin stripes, then overlapped perpendicularly. The voltage is applied only in square areas, that we will call "field-active", where the array is formed; (2) irregular areas are locally melted with optical tweezers until they relax to the regular structure. Because the second approach requires direct intervention of experimenters, it cannot be used for tunable systems where the external electric field should be the only control parameter. The first approach is more desirable as it does not require a direct intervention; however, here we show that as the size of electrode becomes large compared to the characteristic spacing between neighboring defects the regularity of the defect array becomes increasingly unstable. We overcome the intrinsic limitation of the previous method by fabricating continuous electrodes with

Department of Physics and Astronomy, Johns Hopkins University, Baltimore 21218, USA. E-mail: francesca.serra@jhu.edu

† Electronic supplementary information (ESI) available: Fig. S1–S8; Table S1 and Videos S1–S6. See DOI: 10.1039/c8ra08251k

periodic conductivity. We achieve this by etching stripes out of a conductive layer but not completely, in such a way that electrodes are present everywhere but their conductivity is modulated. We can thus apply the vertical electric field everywhere while generating spatially periodic modulation. Thanks to this simple but robust method, the regular array can be extended to arbitrarily large scale. In addition, we show how the presence of patterned electrodes influences the characteristic distance between defects and how this distance can be tuned.

Experimental

Materials and methods

LC mixture. We used the LC compounds CCN-mn (4,4'-dialkyl-(1α,1'α-bicyclohexyl)-4β-carbonitrile, Nematel GmbH & Co. KG) with negative dielectric anisotropy ($\Delta\varepsilon < 0$). The CCN-47 and CCN-55 were mixed in equal proportion so that the mixture was nematic at room temperature. 1 wt% of an ionic salt, tetrabutyl ammonium benzoate (TBABE) was mixed into the LCs. The mixtures were diluted in chloroform and agitated by ultra-

sonication for 20 min. The chloroform was evaporated for 12 hours afterward.[21]

Cells. We prepared several cells with different electrode widths. For patterned electrodes, a positive-type photoresist (Micromposit S1813, Dow) was firstly spin-coated (step 1: 800 rpm for 20 s; step 2: 3000 rpm for 30 s) on indium-tin-oxide (ITO) coated glass substrates and soft-baked at 115 °C for 1 min. The UV light irradiated (~28 mW cm^{-2} for 4.5 s) onto the substrates covered by a chrome mask with designed electrode-pattern, and the substrates were submerged in a developer (Micromposit 351, Dow) for ~30 s. The substrates were then submerged in an acidic etchant (HCl : HNO$_3$: H$_2$O = 1 : 0.1 : 1) until the exposed ITO area was fully etched. For incompletely etched electrodes, we controlled the etching time and monitored the resistivity of the exposed ITO area until the resistivity became 3 orders of magnitude higher than the photoresist covered area. The photoresist residue was removed by acetone thereafter. The homeotropic alignment layer was coated on the patterned electrodes. The substrates were spin-coated (3000 rpm for 30 s) with an amorphous fluoropolymer solution, prepared by mixing
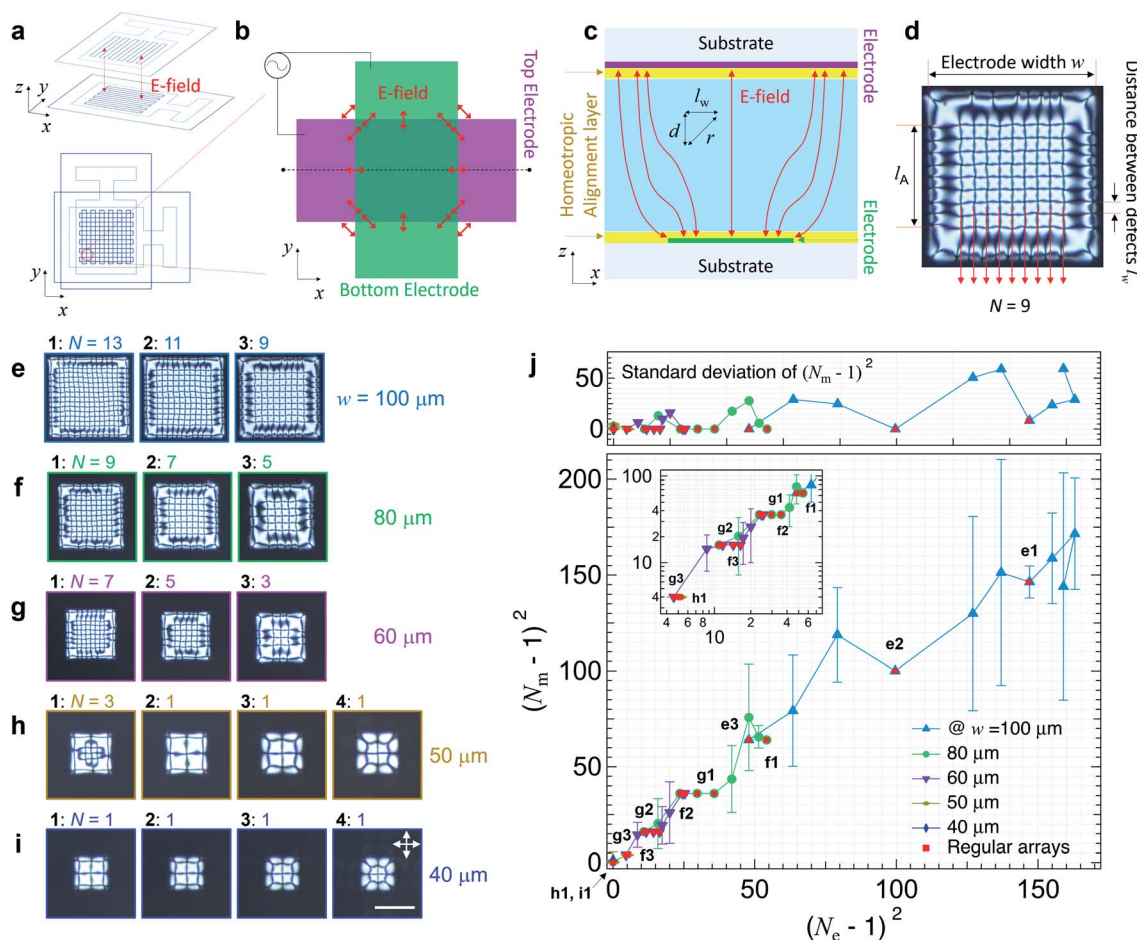

Fig. 1 The electrode-confinement effect and regular arrays. (a) Schematics of the LC cell. (b and c) Schematics of the applied field lines (red arrows) (b) in the $x-y$ and (c) $x-z$ planes (the scales in x- and z-axes are different). (d) Measurable parameters of the array. (e–i) Polarizing optical microscopy (POM) images of defect arrays with different w (see also ESI Videos S2–S6† for sequential images). The scale bar is 50 μm. (j) Measured $(N_m - 1)^2$ with respect to estimated $(N_e - 1)^2 = l_A{}^2 / \left(r^2 - \beta \dfrac{K\pi^2 - \varepsilon V^2}{2f\gamma} \right)$. Upper: the standard deviation of $(N_m - 1)^2$; inset: logarithmic scale where $(N_m - 1)^2 < 100$.

a solute (CTL-809M, Asahi Glass Co.), which contains 9 wt% of CYTOP, into a solution (CT-Solv.180, Asahi Glass Co.) with the ratio 1 : 2 in weight, and then baked (step 1: 70 °C for 30 min; step 2: 120 °C for 30 min) following the protocol in ref. 21. The substrates were assembled while maintaining the cell gap by spacer beads. The empty cell gap was measured by the interferometric method using a UV-VIS spectrometer (Flame, Ocean Optics).

Characterization. The POM images were obtained by using a polarizing optical microscope (Eclipse LV100 POL, Nikon Inc.), and the Polscope microscopy images were obtained by a Phi-Viz Imaging system (Polaviz) on a polarizing optical microscope. The defect arrays were generated by applying AC electric fields in a sinusoidal waveform, $V(t) = V_0 \cos(2\pi f t)$, generated by a waveform generator (DS345, SRS, Inc.) and amplified by a power amplifier (Model 2205, Trek, Inc.). We measured voltage-dependent optical transmittance curves (V–T curves) as well as the threshold voltage V_{th} while fixing f and sweeping V. After measuring the V–T curves and determining the V_{th}, we were able to apply V and f in such a way that all the images had similar brightness. Between each measurement where both V and f were changed, such as those shown in the sequential images (ESI Videos S1–S7†), the voltage was always dropped below the threshold voltage. V and f were then re-adjusted to the new values and the system observed.

Quantification of parameters. The parameters in POM images were evaluated using an image processing software (ImageJ)[26] and systematically obtained by the macro-function and appropriate set of regions of interest (ROIs) in the images. The mean values and error bars were evaluated by considering both x and y axis in 5 different ROIs in the images (ESI Fig. S2†). For estimated $(N_e - 1)^2$ and $l_{w,e}$, measured parameters are V, f, l_A, d, l_w; and the material properties were set as $K = 10^{-11}$ [N], $|\Delta\varepsilon| = 5$, $\varepsilon_0 = 8.85 \times 10^{-12}$ [N V^{-2}], $\gamma = 0.1$ [Pa s].[27]

Results and discussion

We verify the dependency of the characteristic spacing between defects l on the frequency f and the voltage V in our sample (see ESI Fig. S1c–e and Video S1† for sequential images) using a mixture of CCN-47 and CCN-55. The spacing l is proportional to V and inversely proportional to $f^{1/2}$ (ESI Fig. S1d and e†) in the range between $l_{min} \sim 9.5$ and $l_{max} \sim 15$ µm where the thickness is $d \sim 3.7$ µm. The range of allowed spacing strongly depends on d, as reported.[21] However, the arrangement of the defects is irregular, and the single domain order is short range.

We fabricate cells with ITO electrodes patterned in thin stripes and arranged perpendicularly. Strong lateral electric fields form along both polar and azimuthal angles at the electrode edges (Fig. 1a–c). We vary the electrode width from $w = 100$ to 40 µm (Fig. 1e–i) and define parameters as the length of the area l_A containing the regular defect array and the distance between neighboring defects l_w (Fig. 1d). It is immediately evident that l_A does not span the whole width w, and that the defect array encompasses a fraction of the total area. In the most general case, without appropriate tuning of V and f, the

array is still irregular. However, by spanning a wide range of V and f it is possible to find combinations of parameters that produce regular arrays, where $l_w = l_A/(N - 1)$. The measured number of umbilical defects N_m in each row of the array is an odd number whenever arrays are regular. N_m can be visualized in the images as the number of dark vertical lines (Fig. 1d). N_m can be tuned by changing V and f. In transient states between consecutive odd values of N_m, we can observe either dislocations in the defect arrays or randomly disoriented arrays (see ESI Videos S2–S6† for sequential images).

To understand the behavior of the LCs, we first consider the response of both LCs and ions in the system, as outlined in ref.
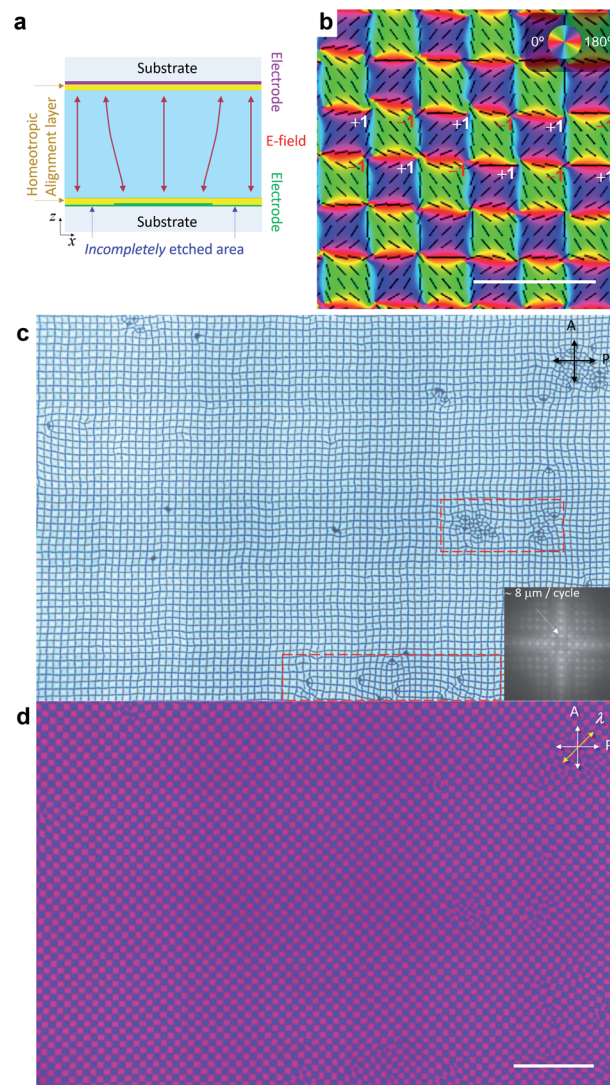

Fig. 2 Incomplete etching for large-scale arrays. (a) The red arrows represent electric field formation in the x–z plane. (b) A PolScope microscopy image of a defect array. The dark lines and the color map represent LC directors. The scale bar is 20 µm. (c and d) POM images (c) without or (d) with a full-wave plate. The array is obtained with $w = 100$ µm, $V = 15$ V, $f = 500$ Hz. The inset is the 2D-FFT of the array in (c). The yellow arrow represents the full-wave-plate. Defects in defect arrays are highlighted in the red-dotted rectangle. The slightly shaded stripes in (c) and (d) correspond to the non-etched parts of the electrodes, while the clearer parts are incompletely etched. The scale bar is 100 µm.

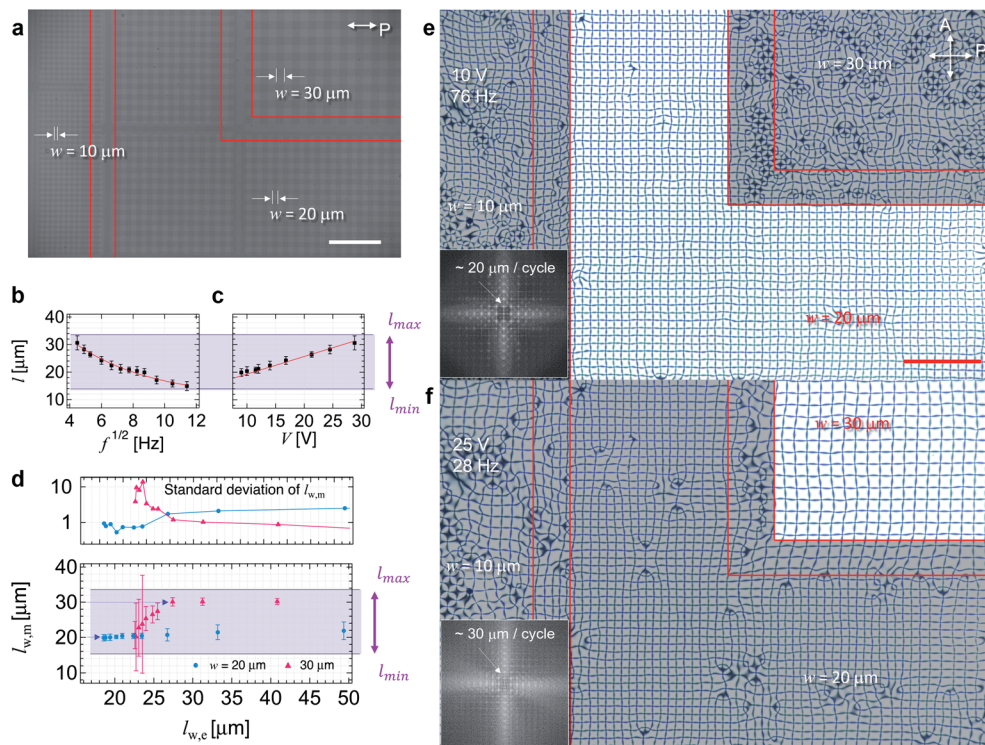**Fig. 3** Control of large-scale arrays. (a) Electrodes with $w = 10, 20$ and 30 μm when LC is homeotropically aligned and no voltage is applied. The red lines indicate boundaries. The scale bar is 200 μm. (b and c) Measured l as a function of (b) f and (c) V, at $d = 7.8$ μm. (d) The measured $l_{w,m}$ and its standard deviation (upper panel) with respect to estimated $l_{w,e} \sim \left(r^2 - \beta \dfrac{K\pi^2 - \varepsilon V^2}{2f\gamma} \right)\left(\dfrac{n}{w} \right)$. The blue-single-headed arrows indicate that the regular array appears where $l_w \sim w$. (e and f) POM images under (e) 10 V at 76 Hz and (f) 25 V at 28 Hz (see ESI Videos S7† for sequential images). The brighter areas highlight regular arrays at $w =$ (e) 20 and (f) 30 μm. Each inset is the 2D-FFT of the regular region. The scale bar is 200 μm.

23–25. The ion and director relaxation times can be determined as $\tau_{ion} = \varepsilon_0 \varepsilon_r / \sigma$ and $\tau_{LC} = \gamma d^2 / (K\pi^2 - \varepsilon V^2)$, respectively, where γ is the LC viscosity. We assume the splay (K_{11}), twist (K_{22}) and bend (K_{33}) elastic constants to be all equal to K; $\varepsilon = \varepsilon_0 \varepsilon_r$; ε_0, ε_r and σ are the vacuum permittivity, the relative permittivity (dielectric constant) and conductivity, respectively.[25] The ion relaxation time is shorter than inverse of field-frequency, that is, $\tau_{ion} < \tau_{LC} \sim (2f)^{-1}$. We consider the director relaxation in the z-axis and x–y plane by the vertical and the lateral components of electric fields, respectively, and introduce the total displacement $r^2 = d^2 + l_w^2$ (inset in Fig. 1c). Thus, $2f = (K\pi^2 - \varepsilon V^2)/\gamma(r^2 - l_w^2)$. In the absence of patterned electrodes and lateral confinement, l_w depends on d, V and f. In our system, we can show that it is affected by w and more specifically by l_A. We measure l_w, l_A and N independently. By replacing $l_w = l_A/(N-1)$, we are able to describe the estimated total number of "squares", *i.e.*, areas between umbilical defects in a regular arrangement, as $(N_e - 1)^2 = l_A^2 / \left(r^2 - \beta \dfrac{K\pi^2 - \varepsilon V^2}{2f\gamma} \right)$, where N_e is the estimated number of defects per line. Here, due to the difficulty in determining a single value for the viscosity γ in this composite system, we leave β as a free parameter. In this way, β can account also for the imprecisions associated with K and ε. We set the material properties as $K = 10^{-11}$ [N], $|\Delta \varepsilon| = 5$, $\varepsilon_0 = 8.85 \times 10^{-12}$ [N V^{-2}], $\gamma = 0.1$ [Pa s].[27] In Fig. 1j, we plot (N_m

$-1)^2$, the measured value, as a function of the estimated value $(N_e - 1)^2$.

Three observations emerge from the plot in Fig. 1j. First, measurements and theory are in a good agreement, confirmed by the fact that the fitting parameter β is fairly close to 1. Second, it is evident that if the set of parameters is close enough to those of a regular array, there is a high energy cost associated with disrupting the array. This is particularly evident in the case of the smaller electrodes. Third, the standard deviation, measured by counting the number of defects over many repetitions of the experiments, increases as the electrode size increases. In other words, as the electrodes get bigger it is harder to get the right set of parameters that will guarantee the regularity of the array.

It is evident that the latter consideration hinders the possibility of using very large electrodes to create arbitrarily large-scale arrays. However, large electrodes would be desirable because that would reduce the effects of edges, where the array is not regular, as shown in ESI Fig. S1d–i and S2.† For large-scale arrays, these edges should be removed. Similarly, we need to find a way to eliminate the "dead" areas, where there are no electrodes.

To overcome this impasse, we etch the electrodes only partially. In this way, the electric field is applied over the entire area while still maintaining a non-zero x–y component at the boundary between non-etched and incompletely-etched parts

(Fig. 2a). The defect array can be thus continuously arranged over a large area (Fig. 2b–d). A PolScope microscopy image can confirm the LC director profile in the x–y plane (Fig. 2b). In Fig. 2, one can still clearly see some dislocations highlighted in the red-dotted rectangles (Fig. 2c). The study of the dynamics of such dislocations is of interest to us, but outside the scope of this paper. Here, instead, we focus on how to eliminate these "defects in defects" in order to make regular arrays.

To enhance the regularity, we use fine electrode patterning. A specially designed photomask allows us to observe the effect of electrodes with $w = 10$, 20, and 30 μm within an area of about a square millimeter (Fig. 3a). We first measure l with plain electrodes, finding that l ranges from $l_{min} \sim 14$ to $l_{max} \sim 35$ μm at $d = 7.8$ μm (Fig. 3b and c). We then proceed to the system which uses incompletely etched electrodes. We see that for this system the regular arrays occur where $l_{w,m} \sim w$, that is, the number of defects n per electrode is 1 (see Fig. S3, ESI†). Here, n is the number of defects per electrode for the incompletely etched electrodes while we use N for the completely etched electrodes. We measure $l_{w,m}$ with $w = 20$ and 30 μm and plot it as a function of $l_{w,e} \sim \left(r^2 - \beta \dfrac{K\pi^2 - \varepsilon V^2}{2f\gamma} \right)\left(\dfrac{n}{w} \right)$, an expected value of l_w obtained with the same procedure used to estimate N_e (Fig. 3d). Here, the same value determined for Fig. 1j is used for the parameter β. A regular array with $l_{w,m} \sim 20$ μm appears in the area covered by electrodes with $w = 20$ μm ($V = 10$ V, $f = 76$ Hz, Fig. 3e), and an array with $l_{w,m} \sim 30$ μm appears when w

$= 30$ μm ($V = 25$ V, $f = 28$ Hz, Fig. 3f) (see ESI Videos S7† for sequential images). In this case, the effect of lateral confinement from the electrodes is more dramatic. For a fixed set of parameters the different size of electrodes leads to significant variations of $l_{w,m}$ from the expected value $l_{w,e}$. In particular, the large confinement exerted by the electrode with $w = 20$ μm is able to keep the $l_{w,m}$ constant at $w = 20$ μm even when $l_{w,e}$ in a "free" system could be much larger. This finding is promising for the creation of bistable systems.

To verify the existence of arrays for wider electrodes, where $n > 1$, we observe and measure the quantities using electrodes with $w = 10$, 20, 30, 40 and 50 μm and $d \sim 3.7$ μm (Fig. 4). By changing $l_{w,e}$ through V and f, we observe the relation of $l_{w,m}$ with respect to w and n (ESI Table S1†). At $w = 10$ μm (Fig. 4a), $n = 1$ and $l_{w,m} \sim 10$ μm is constant for the entire explored range of V and f; at $w = 20$ μm (Fig. 4b), $l_{w,m} \sim 6.7$ μm with $n = 3$ ($l_{w,e} \sim w/n \sim 20/3$ μm); at $w = 30$ μm (Fig. 4c), $l_{w,m} \sim 10$ μm and $n = 3$; at $w = 40$ μm (Fig. 4d), $l_{w,m} \sim 7.9$ or 13.1 μm with $n = 5$ or 3; at $w = 50$ μm (Fig. 4e), $l_{w,m} \sim 7.1$ or 10 μm with $n = 7$ or 5 (see details in ESI Table S1†). The red fonts in Table S1† indicate irregular arrays during the transient states (large images are available in ESI Fig. S4 and S5†). These measurements show an "odd-even" effect. If a regular array can stably form with 10 μm electrodes (Fig. 4a), the same array is not as stable with a 20 μm electrode (Fig. 4b). The reason is intuitive: doubling the number of defects per line does not satisfy the boundary conditions at the electrode edge. One defect with winding number -1 will be next
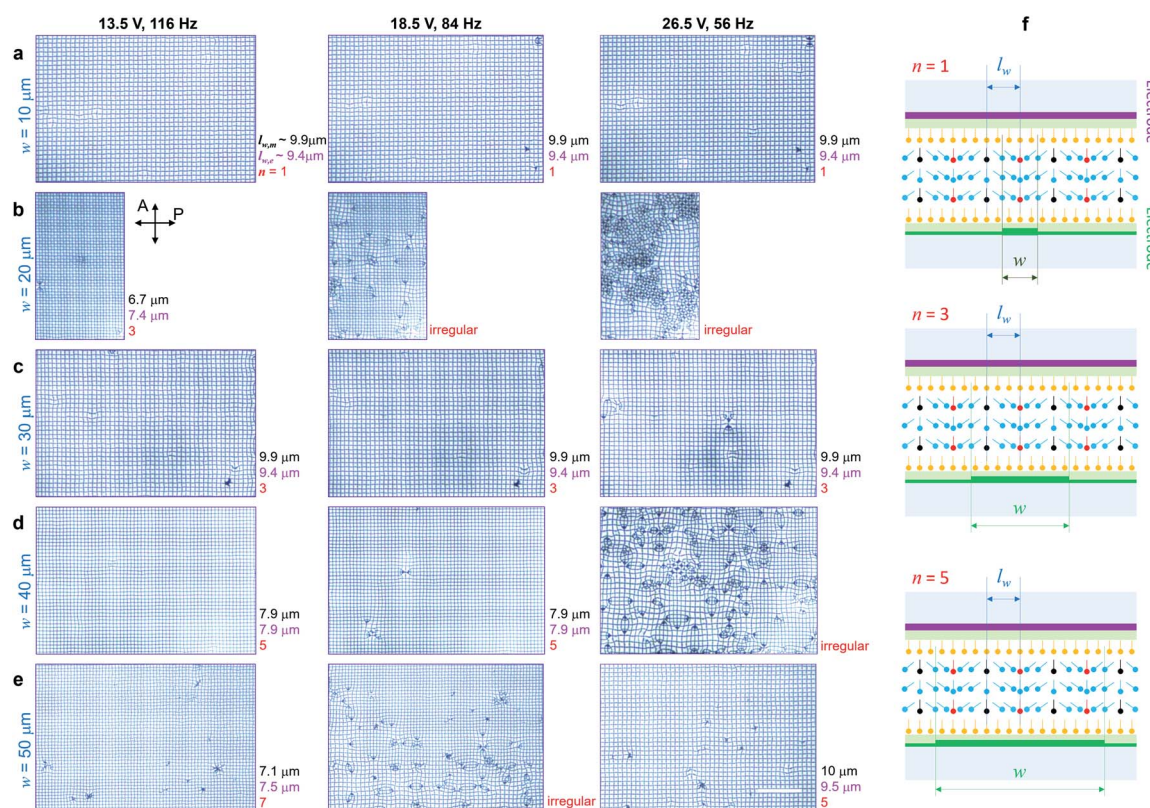

Fig. 4 The size dependence of regular arrays with respect to the electrode width $w =$ (a) 10, (b) 20, (c) 30, (d) 40, and (e) 50 μm. The regular array appears when $l_w = w/n$, where n is an odd number. When w/n is out of the range of l_w or it is in a transient state between odd numbers, the array becomes irregular. The scale bar is 100 μm (large scale images available in ESI Fig. S4 and S5†). (f) Schematics of director fields with $n = 1$, 3, and 5.

to one corner while a defect with winding number +1 will be next to the other. Only adding a third defect on the line will restore the same LC orientation next to the electrode edge (Fig. 4f). As expected, the network formed with the 20 μm electrode is frustrated and easily disrupted, while the network formed with the 30 μm electrode (Fig. 4c) is regular. The same is valid for the 40 and 50 μm electrodes (Fig. 4d and e). This can be seen clearly in the Fourier spectrum of the array, shown in ESI Fig. S7.† We notice, however, that other effects can come into play for large electrodes such as the 50 μm electrodes. The image in the second column in Fig. 4e shows a "transition" between a finer array spacing in the upper part of the figure with $n = 7$ and a coarser array in the lower part of the figure with $n = 5$. This, once again, confirms the importance of using finer electrodes to guarantee the regularity of the array. On the other hand, using wider electrodes can allow for the formation of multi-stable systems with different periodicity. Finally, in this system the only limitations to the size of the array are given by the size of the patterned electrode area (i.e. the area of the photomask) and by the impurities of the surface. We can exactly map the imperfections in our defects arrays onto random impurities on the surface, as shown in ESI Fig. S8.† As these limitations can be easily overcome with cleanroom preparation, these arrays can be extended over areas of many square centimetres, and thus provide a suitable platform for applications.

Conclusions

We investigated how the lateral electric field confinement applied through finely patterned electrodes helps accommodate regular arrays of umbilical defects. We can control the spacing between neighboring defects and show tunable large-scale regular defect arrays solely controllable via electric fields. We study the role of the electrode size in the generation of the regular arrays induced by electric fields using a negative dielectric anisotropy material. The characteristic spacing and the number of defects were defined with respect to the properties of the materials and the other measured physical quantities. We found that the key to have very regular arrays is to use thin electrodes, with sizes comparable to the characteristic distance between the defects. Thanks to the stratagem of incompletely etching the electrodes, we can generate large-scale periodic electric fields that are slightly modulated, thereby producing regular defect arrays with no spatial limitation. In this way, the array is regular and tunable only via electric field, without the need for the direct intervention of the experimenters. This outlines a new route to design large-scale arrays that are self-assembled and tunable, and that can be used as multi-functional devices, optical gratings or as sites for particle assembly.

Conflicts of interest

There are no conflicts to declare.

Acknowledgements

Notes and references

1 G. Krausch and R. Magerle, Adv. Mater., 2002, 14, 1579–1583.
2 S. B. Darling, Prog. Polym. Sci., 2007, 32, 1152–1204.
3 J. Zhang, Y. Li, X. Zhang and B. Yang, Adv. Mater., 2010, 22, 4249–4269.
4 V. Lotito and T. Zambelli, Adv. Colloid Interface Sci., 2017, 246, 217–274.
5 I. W. Hamley, Angew. Chem., Int. Ed., 2003, 42, 1692–1712.
6 Y. H. Kim, D. K. Yoon, H. S. Jeong, J. H. Kim, E. K. Yoon and H. T. Jung, Adv. Funct. Mater., 2009, 19, 3008–3013.
7 M. Wang, Y. Li and H. Yokoyama, Nat. Commun., 2017, 8, 388.
8 F. Serra, K. C. Vishnubhatla, M. Buscaglia, R. Cerbino, R. Osellame, G. Cerullo and T. Bellini, Soft Matter, 2011, 7, 10945.
9 S. Shojaei-Zadeh and S. L. Anna, Langmuir, 2006, 22, 9986–9993.
10 I. Dierking, O. Marshall, J. Wright and N. Bulleid, Phys. Rev. E, 2005, 71, 061709.
11 P. J. Ackerman, Z. Qi and I. I. Smalyukh, Phys. Rev. E: Stat., Nonlinear, Soft Matter Phys., 2012, 86, 021703.
12 R. Barboza, U. Bortolozzo, G. Assanto, E. Vidal-Henriquez, M. G. Clerc and S. Residori, Phys. Rev. Lett., 2013, 111, 093902.
13 P. J. Ackerman, Z. Qi, Y. Lin, C. W. Twombly, M. J. Laviada, Y. Lansac and I. I. Smalyukh, Sci. Rep., 2012, 2, 414.
14 F. Serra, M. A. Gharbi, Y. Luo, I. B. Liu, N. D. Bade, R. D. Kamien, S. Yang and K. J. Stebe, Adv. Opt. Mater., 2015, 3, 1287–1292.
15 M. E. McConney, A. Martinez, V. P. Tondiglia, K. M. Lee, D. Langley, I. I. Smalyukh and T. J. White, Adv. Mater., 2013, 25, 5880–5885.
16 T. H. Ware, M. E. McConney, J. J. Wie, V. P. Tondiglia and T. J. White, Science, 2015, 347, 982–984.
17 Y. Xia, G. Cedillo-Servin, R. D. Kamien and S. Yang, Adv. Mater., 2016, 28, 9637–9643.
18 B. S. Murray, R. A. Pelcovits and C. Rosenblatt, Phys. Rev. E: Stat., Nonlinear, Soft Matter Phys., 2014, 90, 052501.
19 P. Pieranski, E. Dubois-Violette and E. Guyon, Phys. Rev. Lett., 1973, 30, 736–739.
20 C. Peng, Y. Guo, C. Conklin, J. Viñals, S. V. Shiyanovskii, Q. H. Wei and O. D. Lavrentovich, Phys. Rev. E: Stat., Nonlinear, Soft Matter Phys., 2015, 92, 052502.
21 Y. Sasaki, V. S. R. Jampani, C. Tanaka, N. Sakurai, S. Sakane, K. V. Le, F. Araoka and H. Orihara, Nat. Commun., 2016, 7, 13238.
22 L. K. Migara and J.-K. Song, NPG Asia Mater., 2018, 10, e459.
23 W. Helfrich, J. Chem. Phys., 1969, 51, 4092–4105.
24 E. Dubois-Violette, P. G. d. Gennes and O. Parodi, J. Phys., 1971, 32, 305–317.
25 A. Hertrich, W. Decker, W. Pesch and L. Kramer, J. Phys. II, 1992, 2, 1915–1930.
26 C. A. Schneider, W. S. Rasband and K. W. Eliceiri, Nat. Methods, 2012, 9, 671–675.
27 S. Dhara and N. V. Madhusudana, Phase Transitions, 2008, 81, 561–569.